



1 **In-situ Observation of Riming in Mixed-Phase Clouds using the PHIPS**
2 **probe**

3 Fritz Waitz^a Martin Schnaiter^{a,b} Thomas Leisner^a Emma Järvinen^a

4 ^a *Institute of Meteorology and Climate Research, Karlsruhe Institute of Technology, Karlsruhe,*
5 *Germany* ^b *schnaiTEC GmbH, Bruchsal, Germany*



7 ABSTRACT: Mixed-phase clouds consist of both supercooled liquid water droplets and solid ice
8 crystals. Despite having a significant impact on Earth's climate, mixed-phase clouds are poorly
9 understood and not well represented in climate prediction models. One piece of the puzzle is
10 understanding and parameterizing riming of mixed-phase cloud ice crystals, which is one of the
11 main growth mechanisms of ice crystals via the accretion of small, supercooled droplets. Especially
12 the extent of riming on ice crystals smaller than $500\ \mu\text{m}$ is often overlooked in studies - mainly
13 because observations are scarce. Here, we investigated riming in mixed-phase clouds during three
14 airborne campaigns in the Arctic, the Southern Ocean and US east coast. Riming was observed
15 from stereo-microscopic cloud particle images recorded with the Particle Habit Imaging and Polar
16 Scattering (PHIPS) probe. We show that riming is most prevalent at temperatures around -7°C ,
17 where, on average, 43% of the investigated particles in a size range from $100 \leq D \leq 700\ \mu\text{m}$ showed
18 evidence of riming. We discuss the occurrence and properties of rimed ice particles and show
19 correlation of the occurrence and the amount of riming with ambient meteorological parameters.
20 We show that riming fraction increases with ice particle size ($<20\%$ for $D \leq 200\ \mu\text{m}$, $35\text{-}40\%$ for
21 $D \geq 400\ \mu\text{m}$) and liquid water content (25% for $\text{LWC} \leq 0.05\ \text{g m}^{-3}$, up to 60% for $\text{LWC} = 0.5\ \text{g m}^{-3}$).
22 We investigate the ageing of rimed particles and the difference between "normal" and "epitaxial"
23 riming based on a case study.



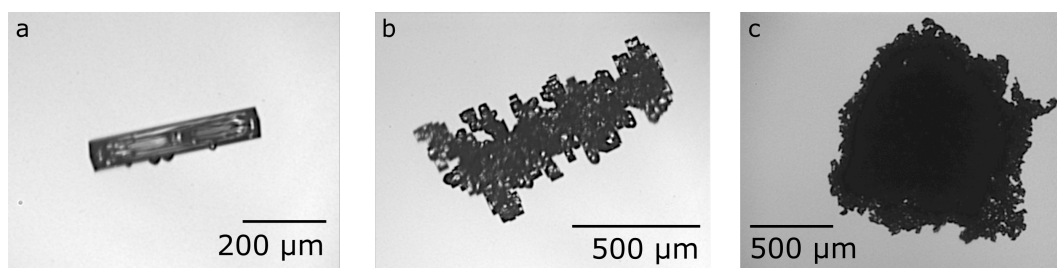
24 1. Introduction

25 Mixed-phase clouds (MPCs), consisting of both supercooled liquid droplets and ice particles,
26 play a major role in the life cycle of clouds and the radiative balance of the Earth (e.g. Korolev et al.
27 2017). Despite their widespread occurrence, mixed-phase cloud processes are still rather poorly
28 understood and represent a great source of uncertainty for climate predictions (e.g. McCoy et al.
29 2016).

30 One important microphysical process in MPCs is *riming*, i.e. the accretion of small supercooled
31 liquid droplets on the surface of ice particles (see example in Fig. 1a). Besides vapor deposition
32 and aggregation, it is one of the three main growth modes.

33 Riming can be divided into two (not always easily distinguishable) sub-topics: riming of small
34 ice particles (diameter $D \approx 100 - 1000 \mu\text{m}$) in clouds and riming of large ($1000 \lesssim D \lesssim 5000 \mu\text{m}$)
35 precipitating ice, graupel and snow particles. The typical life-cycle of an exemplary rimed particle
36 is usually as follows: The ice particle is formed, following growth via vapor deposition until
37 the particle has reached a critical minimum size for riming (depending on shape and habit, e.g.
38 $D \geq 60 \mu\text{m}$ for columns, (e.g. Ono 1969; Ávila et al. 2009)). If liquid droplets are present in large
39 enough numbers, the ice particle starts collecting supercooled droplets (around $D = 10 - 40 \mu\text{m}$,
40 e.g. Harimaya (1975)) that freeze on the particle's surface until gravitational settling becomes
41 efficient. Whilst falling, the ice particle can accrete even more droplets and grow further until it
42 reaches the ground as graupel.

43 Ice particle growth, both in size and mass, can ultimately change cloud lifetime and radiative
44 properties. The scavenging of supercooled liquid water affects droplet size distribution and number
45 concentration and thus liquid water content as well as aerosol concentration (Baltensperger et al.
46 1998; Hegg et al. 2011). Also, splintering during the riming process can initiate secondary ice
47 formation, thus leading to the formation of new ice particles known as the *Hallett-Mossop-process*
48 (e.g. Hallett and Mossop 1974; Korolev et al. 2020; Field et al. 2017). Since rimed ice particles
49 are of higher mass and more compact compared to unrimed particles, their fall speed and terminal
50 velocity are increased (Locatelli and Hobbs 1974; Lin et al. 2011; Garrett and Yuter 2014).
51 Furthermore, riming leads to increased surface roughness and complexity, and hence affects the
52 ice particles' radiative properties, as shown in e.g. Schnaiter et al. (2016); Järvinen et al. (2018);
53 Järvinen et al. (2021).



54 FIG. 1. Example of a (a) slight "normally" rimed , (b) heavily "epitactically" rimed column and (c) a graupel
55 particle captured by the PHIPS probe during the IMPACTS campaign.

56 In principle, riming can occur everywhere where ice particles and supercooled droplets coexist.
57 The riming efficiency of an ice particle is a function of (i) its collection efficiency and (ii) the
58 number of supercooled droplets, integrated over (iii) the time the ice particle spends in the cloud and
59 during precipitation. These three quantities depend on numerous parameters including temperature
60 (Kneifel and Moisseev 2020), habit and size of the ice particle (Ono 1969; Wang and Ji 2000; Ávila
61 et al. 2009), size of the supercooled droplets (Saleeby and Cotton 2008) as well as turbulence and
62 vertical velocity (Herzegg and Hobbs 1980; Garrett and Yuter 2014).

63 In recent years, multiple studies have used radar measurements to retrieve information about
64 snow and riming density based on their vertical Doppler velocity (Mosimann et al. 1993; Leinonen
65 and Szyrmer 2015; Leinonen et al. 2018; Mason et al. 2018; Kneifel and Moisseev 2020). Those
66 methods proved to be fit to determine the riming state of large, precipitating snow and graupel
67 particles. However, they cannot resolve the fine structure of small or freshly rimed ice particles
68 inside clouds if the radar signal is dominated by large graupel particles in the size range $D =$
69 $1 - 10$ mm. In-situ studies with high-resolution cloud imaging probes investigating the properties
70 of individual rimed particles sampled directly in the cloud, however, are scarce. The difficulty is
71 to resolve riming features and discriminate between rimed and irregular particles. Furthermore,
72 analysis of particle images is quite complex and hence automate and manual assessment of particle
73 properties is very laborious. Consequently, the riming of ice particles is often times poorly or
74 not at all represented in climate prediction models. So far, the exact processes influencing the
75 riming of could particles are not well understood. A deterministic parameterization of when and
76 where to expect how much riming does not exist. Most models account for the riming degree only
77 in the sense of a *subtype* for hydrometeors (e.g. *cloud ice*, *graupel*, *snow*, COSMO, Blahak and



78 Seifert (2015), <http://www.cosmo-model.org/>). Furthermore, riming is neglected completely in
79 most Arctic model studies (e.g. Fan et al. 2011; Ovchinnikov et al. 2014; Stevens et al. 2018).

80 In this work, we investigate riming of ice particles using the Particle Habit Imaging and Polar
81 Scattering (PHIPS) probe. PHIPS is an aircraft-mounted cloud probe acquiring stereo-microscopic
82 images and corresponding angular scattering functions of single cloud particles in the size range
83 $D = 20 - 700 \mu\text{m}$ and $D = 50 - 700 \mu\text{m}$ for ice and droplets, respectively. With its high optical
84 resolution and single particle measurements, PHIPS is well suited to investigate detailed features
85 like riming of individual ice particles. We present microphysical observations of ice particles from
86 three field campaigns investigating high latitude MPC. In section 2, we give an overview of the three
87 field campaigns as well as a brief introduction of the PHIPS probe and its data analysis methods.
88 Combining the data from these three field campaigns, an extensive data-set observing ice particles
89 of various size, habit and riming state has been acquired. In section 3, we present a statistical
90 analysis of the correlation with ambient conditions of rimed particles for different scales of riming.
91 We estimate the minimum size of rimed particles as well as droplets, confirming the results of
92 previous laboratory studies. Further, we highlight various riming features such as one-sided rimed
93 plates or "*ice lollies*" (Keppas et al. 2017). One particularly interesting observation is ice particles
94 carrying small, faceted rime oriented to the crystalline axis of the host particle. Such particles
95 have been observed before (Korolev et al. 2020) but their occurrence and properties have not been
96 studied comprehensively. This type of riming, which we call *Epitaxial Riming* and which is e.g.
97 shown in Fig. 1b, will be analyzed in detail in section 4 including a case study showing the typical
98 step-by-step evolution of epitaxially rimed particles.

99 2. Methods and Experimental Data Set

100 a. Campaigns

101 In this work, we use experimental in-situ data gathered during three airborne field campaigns:

- 102 1. ACLOUD - Arctic CLOUD Observations Using airborne measurements during polar Day,
103 May/June 2017 based in Svalbard (Spitsbergen, Norway) with the AWI Polar6 aircraft,



104 2. SOCRATES - Southern Ocean Clouds, Radiation, Aerosol Transport Experimental Study,
105 Jan/Feb 2018 based in Hobart (Tasmania, Australia) with the NCAR Gulfstream-V aircraft
106 and

107 3. IMPACTS - Investigation of Microphysics and Precipitation for Atlantic Coast-Threatening
108 Snowstorms, Jan/Feb 2020 based in Wallops (VA, USA) with the NASA P3 aircraft.

109 An overview of the meteorological and microphysical conditions as well as the instrumentation
110 during those campaigns can be found in Knudsen et al. (2018) and Wendisch et al. (2019) for
111 ACLOUD, McFarquhar et al. (2019) for SOCRATES and McMurdie et al. (2019) for IMPACTS.
112 The sampling during those three campaigns includes a wide variety of different cloud conditions:
113 warm clouds, supercooled liquid clouds, ice clouds and mixed-phase clouds. Clouds sampled
114 ranged in altitude from boundary layer clouds below 200 m to mid-level clouds between 4000 m
115 and 6000 m asl. Temperatures ranged from -20 to +5°C during ACLOUD, -35 to +5°C during
116 SOCRATES and -32 to +9°C during IMPACTS. The sampled ice particles covered a wide range
117 of different particle shapes and habits (columns, plates, needles, bullet rosettes, dendrites and
118 irregulars, including rough, rimed and pristine particles) as well as sizes from $D = 20 - 700 \mu\text{m}$. The
119 instrumentation on the three aircraft included cloud particles probes such as the SID-3 (*Small Ice*
120 *Detector Mk. 3*), CDP (*Cloud Droplet Probe*, DMT, Longmont, USA), CIP (*Cloud Imaging Probe*,
121 DMT, Longmont, USA) and PIP (*Precipitation Imaging Probe*, DMT, Longmont, USA) during
122 ACLOUD, 2D-C, 2D-S (*Two-dimensional Stereo Probe*, *Two-dimensional Cloud Probe*, SPEC Inc.,
123 Boulder, USA) and CDP during SOCRATES and 2D-S, CDP and CPI (*Cloud Particle Imager*,
124 SPECinc, Boulder, CO, USA) during IMPACTS. Due to the variability of the meteorological
125 conditions and sampled particles, the data gathered during these three campaigns provide a suitable
126 and representative data set for a comprehensive characterization of riming in mixed-phase clouds.
127 All data cited in this work can be found in the corresponding data bases for the three campaigns:
128 Ehrlich et al. (2019) for ACLOUD, EOL (2018) for SOCRATES, McMurdie et al. (2019) for
129 IMPACTS.

130 *b. The PHIPS Probe*

131 PHIPS is designed to investigate the microphysical and light scattering properties of cloud par-
132 ticles. It produces microscopic stereo-images whilst simultaneously measuring the corresponding



133 angular scattering function for the angular range from 18° to 170° for single cloud particles. More
134 information and a detailed characterization of the PHIPS setup and instrument properties can be
135 found in depth in Abdelmonem et al. (2016) and Schnaiter et al. (2018). From the stereo images,
136 single-particle microphysical features such as e.g. area equivalent diameter or aspect ratio, can
137 be obtained. The image analysis algorithm is explained in depth in Schön et al. (2011). Based
138 on the single-particle's angular scattering function, the thermodynamic phase and the scattering
139 equivalent diameter can be derived as explained in Waitz et al. (2021).

140 For ACLOUD and SOCRATES, the instrument settings were set to measure single cloud particles
141 in a size range from $50 \mu\text{m} \leq D \leq 700 \mu\text{m}$ and $20 \mu\text{m} \leq D \leq 700 \mu\text{m}$ for droplets and ice particles,
142 respectively. The image acquisition rate of the microscopic system was limited to 3 Hz in these
143 campaigns, while single-particle scattering data could be acquired up to a maximum rate of 3.5 kHz.
144 The magnification settings of the cameras corresponded to an optical resolution of approximately
145 $3.3 \mu\text{m}$. Since PHIPS characterizes individual particles, it has a narrow sensitive area (A_{sens}). As
146 discussed in Waitz et al. (2021), A_{sens} is size dependent (e.g. $A_{\text{sens}} = 0.5 \text{ mm}^2$ for ice particles with
147 $D = 200 \mu\text{m}$). Assuming a relative flight speed of $v_s = 150 \text{ m s}^{-1}$, this corresponds to a sampling
148 volume of $V_{\text{sens}} = A_{\text{sens}} \cdot v_s = 0.08 \text{ L s}^{-1}$. During IMPACTS, the scientific focus was on larger ice
149 crystals so the trigger threshold as well as the magnification were increased to trigger only particles
150 larger than $D \geq 100 \mu\text{m}$ for droplets and $D \geq 40 \mu\text{m}$ for ice. The magnification settings of the
151 cameras corresponded to an optical resolution of approximately $4 \mu\text{m}$ and the maximum camera
152 acquisition rate was varied between 3 to 10 Hz, which corresponds to a maximum spatial resolution
153 of roughly one stereo-image per 15 m.

154 *c. Manual Image Classification*

155 All PHIPS stereo-images from the ACLOUD and SOCRATES data-set were visually classified
156 into seven habit classes: (i) plate-like particles (single plates, sectored plates, skeleton plates and
157 side planes), (ii) columnar particles (solid columns, hollow columns and sheaths), (iii) needles,
158 (iv) frozen droplets, (v) bullet rosettes, (vi) graupel, and (vii) irregular particles. In addition
159 to the habits, the particles were assigned the attributes (i) aggregate, (ii) rimed or (iii) pristine.
160 The distribution of the different particle habits are shown in the SI (Figs. S1 and S2) for the two
161 campaigns. An overview of the riming fraction per habit is shown in Fig S3.



162 In a next classification step, a subset of the well classified particles was again visually classified
163 further regarding their riming features. The second classification step was performed only for
164 particles larger than $100\ \mu\text{m}$ sampled at a temperature $>-17^\circ\text{C}$. Smaller particles were almost
165 exclusively small irregulars whose riming state could not be classified with certainty due to the
166 limited optical resolution and almost no riming was observed at lower temperatures, see Fig.2a.

167 Particles were classified regarding their surface riming degree (SRD) as (i) unrimed (SRD = 0%,
168 no visible riming), (ii) slightly rimed (SRD < 25%, a few scattered droplets on the particle's
169 surface), (iii) moderately rimed ($25\% \leq \text{SRD} \leq 50\%$, up to half of the particle's surface is covered
170 by droplets), (iv) heavily rimed ($50\% < \text{SRD} \leq 100\%$, most or all of the particle's surface is covered
171 by rime) as well as (v) graupel (SRD $\gg 100\%$, the whole particle surface is covered by multiple
172 layers of rime, so that the structure of the underlying particle is no longer recognizable). This
173 classification approach is similar to the definition of riming degree used in previous studies such
174 as Magono and Lee (e.g. 1966); Brintjes et al. (e.g. 1987); Mosimann et al. (e.g. 1993, 1994);
175 Mosimann (e.g. 1995). Also, the attributes (i) sublimated, (ii) one sided riming and (iii) epitaxial
176 riming (which will be explained in detail in section 4) were assigned.

177 The remaining data-set includes 3,957 particles from ACLOUD and 1,413 from SOCRATES.
178 Examples of particles classified in the different categories are shown in the following section.
179 Manual classification was not applied for the complete IMPACTS data set due to large number of
180 ice particle images (over 250,000 images were acquired). Therefore, only the set of images used
181 for the case study presented in section 4 was manually inspected.

182 **3. Statistical Analysis and Correlation with Ambient Conditions**

183 In general, the average number of rime found on an ice particle is calculated as the integrated
184 riming rate over the particle trajectory. The riming rate is a function of the relative flux of available
185 droplets and hence droplet number concentration and relative velocity with respect to the ice
186 particle. Further, it is dependent on the collision probability (and hence the cross sections of ice
187 particles and droplets) as well as on the collection efficiency, i.e. the probability that a colliding
188 droplet sticks as rime. The trajectory of the ice particle and thus the time it spends in the cloud is
189 dependent on its mass and the vertical (updraft) velocity.

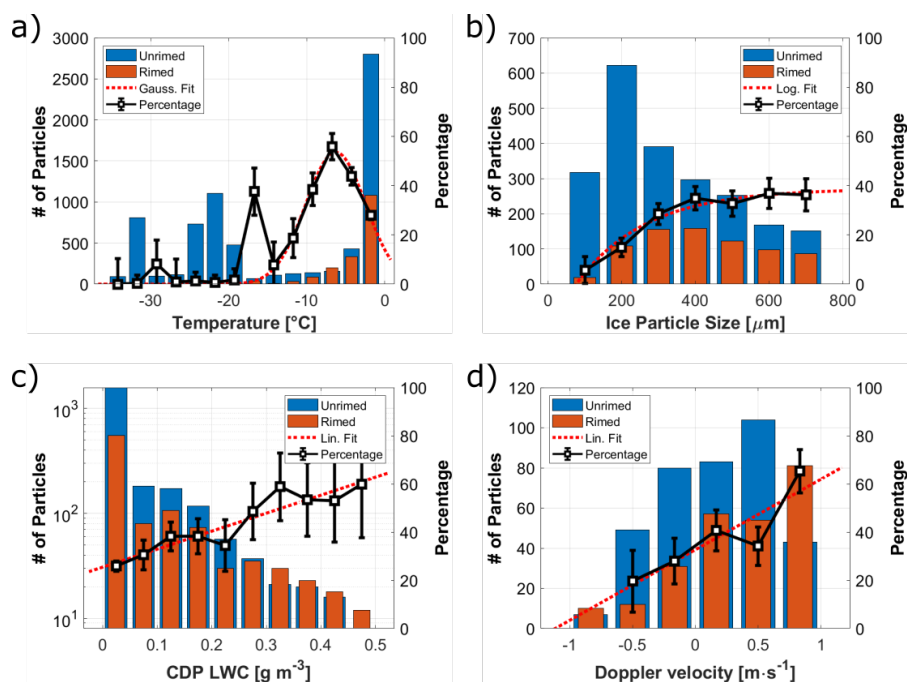


190 It is not possible to know each of those parameters for each particle at every given moment.
191 Hence, as already mentioned above, such detailed description of riming on a particle-by-particle
192 basis is not present in current climate prediction models and riming is only accounted for in terms of
193 graupel and snow and rarely for smaller, less densely rimed particles. Here, we investigate riming
194 of sub-millimeter ice particles based on experimental data and correlate the relative occurrence of
195 rimed and unrimed ice particles with ambient meteorological parameters. Note that the measured
196 conditions do not necessarily represent the environment where the particles were rimed but rather
197 where they were sampled.

198 This statistic is based on 5,370 manually classified images from the ALOUD and SOCRATES
199 campaign. Fig. 2a shows the correlation of riming fraction and ambient temperature. Here, "riming
200 fraction" refers to the relative amount of rimed particles compared to total amount of classified
201 ice particles (rimed + unrimed). Most riming was observed in a temperature range between
202 $-10^{\circ}\text{C} \leq T \leq 0^{\circ}\text{C}$ where up to almost 50% of all ice particles were rimed. The high riming fraction
203 around -17°C is due to a very high rimed fraction during a single cloud segment of RF09 of
204 SOCRATES. It is based on a low number of total particles and is therefore not assumed to be a
205 generalizable feature. The corresponding fit parameters for all histograms are shown in Table 1.

215 For the following analysis, apart from Fig. 2a, only particles sampled at $T \geq -17^{\circ}\text{C}$ are considered.
216 Fig. 2b shows riming statistics as a function of ice particle's area equivalent diameter retrieved from
217 the stereo-microscopic images. It can be seen that the percentage of rimed particles increases with
218 particle size. The riming fraction increases from below 5% for particles smaller than $D_{\text{im,A}} \leq$
219 $150\ \mu\text{m}$ to over 35% for particles larger than $D_{\text{im,A}} \geq 400\ \mu\text{m}$. Above that, the riming fraction
220 is only weakly dependent on particle size. The smallest ice particle where riming was observed
221 was a column with an area equivalent diameter of $D_{\text{im,A}} = 116.1\ \mu\text{m}$ and maximum dimension
222 $D_{\text{im,max}} = 193.7\ \mu\text{m}$ (shown in Fig. S8 in the SI). This is a larger riming onset size compared to
223 e.g. Ono (1969); Ávila et al. (2009)) who reported a critical minimum diameter of $D \geq 60\ \mu\text{m}$ for
224 riming on columns collected via glass slides and analyzed by optical microscopy.

225 The correlation of riming fraction and cloud liquid water content (LWC) measured by the CDP is
226 shown in Fig. 2c. The riming fraction increases from 25% in cloud segments with low LWC below
227 $0.05\ \text{g m}^{-3}$ to 60% for $\text{LWC} \geq 0.5\ \text{g m}^{-3}$. Rimed droplets had a size around roughly $D_{\text{max}} \approx 20$
228 and $50\ \mu\text{m}$ as shown in Figs. 3a,b for two exemplary particles. This is in agreement with results



206 FIG. 2. Histograms showing the absolute number of classified unrimed (blue) and rimed (red) particles during
 207 ACLOUD and SOCRATES as well as the riming fraction (relative percentage $n_{\text{rimed}}/n_{\text{all}}$, black, right axis) in
 208 correlation with different ambient parameters: Temperature (a), area-eq. diameter of the underlying ice particle
 209 measured by PHIPS (b), CDP liquid water content (c) and vertical HCR Doppler velocity (d). The red dotted
 210 line shows a fit to the riming fraction (see text). The corresponding fit parameters for all histograms are shown
 211 in Tab. 1. The statistical uncertainty bars correspond to the number of particles per bin ($n^{-1/2}$). Only bins with
 212 $n \geq 20$ are considered for the fit. Correlation plots with further parameters (CDP mean droplet diameter, ambient
 213 vertical velocity, relative cloud height, supersaturation with respect to ice), which show only a weak dependency
 214 are shown in Fig. S4 in the SI.

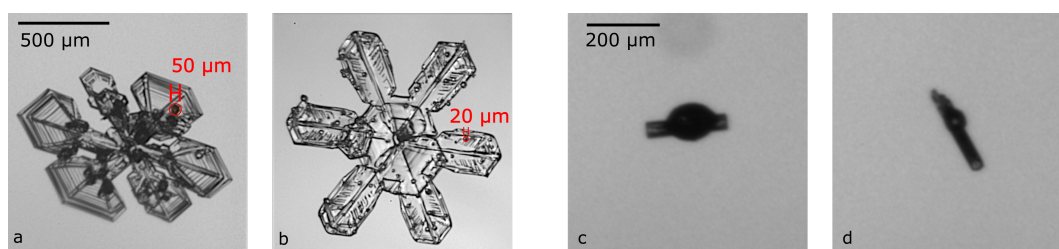
TABLE 1. Fit parameters to the riming percentage histograms shown in Fig. 2.

		Fit function	R ²
Temperature		$y = -0.952 x^2 - 12.2 x + 11.9$	0.940
Ice particle diameter	(PHIPS)	$y = 38.7 - \exp[-52.8 (x-769)]$	0.964
Liquid water content	(CDP)	$y = 74.7 x + 25.5$	0.863
Vertical Doppler velocity	(HCR)	$y = 29.3 x + 32.7$	0.790

229 presented by e.g. Kikuchi and Uyeda (1979); Harimaya (1975), who reported sizes of rimed
 230 droplets between 10 and 60 μm . Comparison with CDP mean droplet diameter showed a slight



231 correlation with a maximum riming fraction at $D_{\text{drop, mean}} = 20 \mu\text{m}$ (see Fig. S4f in the SI). Figs. 3c,d
232 show drizzle-rimed ice (*ice lollies*). Such contact freezing of relatively large droplets compared to
233 the size of ice particle was reported by (Uyeda and Kikuchi 1978; Keppas et al. 2017). We also
234 see this in our data set, but there are only very few cases. Due to the low number, no correlation
235 with sampled PHIPS drizzle droplet concentration was found and no detailed statistical analysis
236 was conducted.



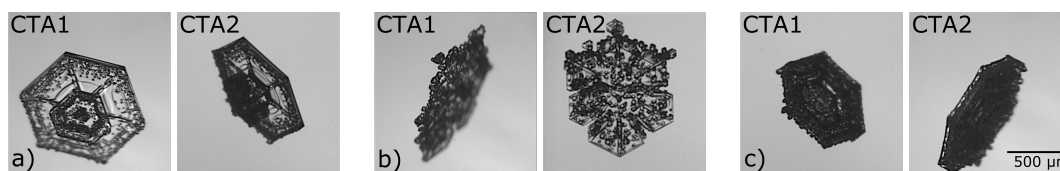
237 FIG. 3. Exemplary rimed particles showing the size of rimed droplets on the surface (a, b) and drizzle rimed
238 ice (*ice lollies*, c,d).

239 Fig. 2d shows the correlation with the Doppler radial velocity measured by the HIAPER cloud
240 Radar (HCR, UCAR/NCAR-EOL (2018)), which is the sum of vertical wind velocity and particle
241 fall speed, corrected by the vertical motion of the aircraft. Negative velocity corresponds to
242 downward direction, positive to updrafts. Since the HCR has a dead zone of 145 m around the
243 aircraft in which data are not usable, there is no data available at the location of the aircraft. One
244 data point corresponds to the average over the whole vertical column. HCR data are only available
245 for the SOCRATES campaign. The HCR was typically rotated to point in zenith direction when
246 flying beneath or ascending through boundary layer clouds and nadir at other times. It can be seen,
247 that there is a clear trend of increasing positive (upward) Doppler velocity with riming fraction.
248 Due to the updraft, the ice particles remain in the cloud longer and hence the probability that they
249 collide with droplets increases. Previous studies have reported increased fall speeds for rimed
250 particles (Locatelli and Hobbs 1974; Lin et al. 2011; Garrett and Yuter 2014) which indicates that
251 the particles are still in the cloud and not yet precipitating.

252 The measurement of ambient vertical velocity around the aircraft shows a slight correlation
253 towards both higher positive and negative values (see Fig. S4h in the SI). This could indicate a
254 correlation with turbulent air motion, as riming is expected to be more likely if particles remain



255 longer in the cloud, having a longer total travel path and hence a higher chance of collecting
256 droplets. However, at the same time, a lot of one sided rimed plates were observed during the
257 campaigns (see Fig. 4), which would be unlikely if all riming would necessarily be correlated
258 with turbulent air motion. This confirms observations of fallen snow by Ono (1969); Rango et al.
259 (2003). Roughly 15% of all plates at warm temperatures $T > -10^{\circ}\text{C}$ are one-sided (see Fig. S7a
260 and the corresponding discussion in the SI) and almost none at colder temperatures.



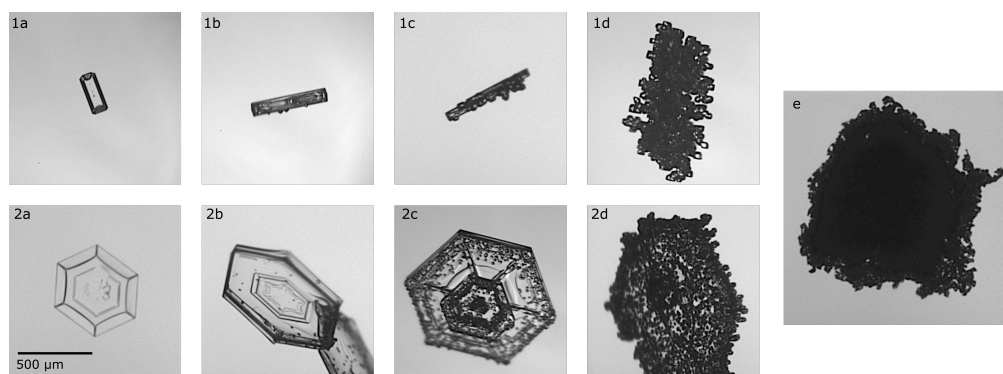
261 FIG. 4. Three exemplary one-sided rimed particles shown from different perspectives by the two camera
262 telescope assemblies (CTA1 and CTA2). Note that the particle orientation in the stereo image does not reflect
263 the orientation within the cloud.

264 No significant correlation (R^2 below 0.5) or only very minor dependency of riming fraction and
265 CDP droplet number concentration, CDP mean droplet diameter, ambient vertical velocity, relative
266 cloud height and supersaturation with respect to ice were found. The corresponding plots are
267 shown in Fig. S4 in the SI.

268 *a. Riming Degree*

269 All rimed ice particles were manually classified concerning their *riming degree*, i.e. their
270 estimated surface riming degree (SRD) (see Sec. c). This classification was done manually based
271 on visual inspection of the particle's individual stereo-images. Exemplary particles are shown in
272 Fig. 5.

276 Fig. 6 shows the relative distribution of SRD with three ambient parameters: temperature
277 (Fig. 6a), ice particle area equivalent diameter (Fig. 6b) and vertical Doppler velocity (Fig. 6c).
278 A correlation is seen between temperature and SRD. At colder temperatures ice particles are more
279 heavily rimed. At temperatures $T \leq -15^{\circ}\text{C}$, more than 80% of all rimed particles are heavily rimed
280 or graupel, whereas most slightly rimed particles are found at warm temperatures between -5 and
281 0°C . The relative fraction of heavily rimed particles is only moderately temperature dependent.



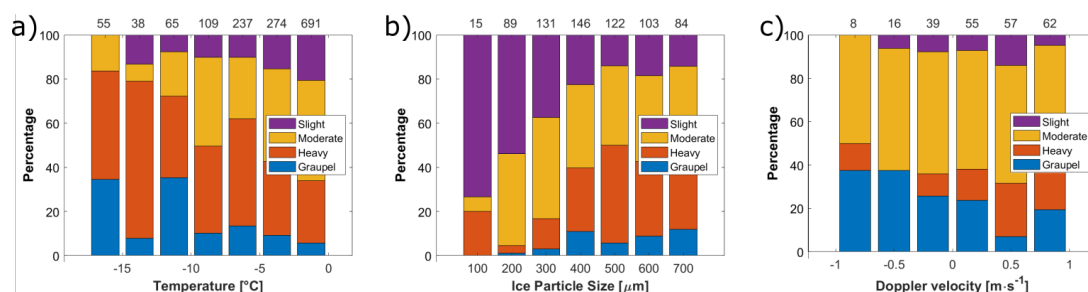
273 FIG. 5. Examples of (1) columnar particles and (2) plates with different degrees of riming depending on the
274 surface riming degree (SRD): unrimed (a, SRD = 0%), slightly rimed (b, $0\% < \text{SRD} < 25\%$), moderately rimed
275 (c, $25 \leq \text{SRD} \leq 50\%$), heavily rimed (d, $50\% < \text{SRD} \leq 100\%$) and graupel particle (e, $\text{SRD} \gg 100\%$).

282 A positive correlation is also visible between SRD and ice particle size: Most small particles
283 around $D_{\text{im},A} \leq 250 \mu\text{m}$ show only slight riming whereas heavy riming is mostly found on larger
284 particles. These typically large graupel particles correlate with an increased negative (downwards)
285 Doppler velocity (Fig. 6c) as they are almost spherical and hence more densely packed compared
286 to aspherical ice particles. This is in agreement with Doppler radar studies presented by Mosimann
287 (1995). However, apart from that, no correlation of SRD with vertical Doppler velocity is visible.
288 The weak but positive trend of SRD and downward Doppler velocity presented by Mosimann
289 (1995) is not seen here. A possible explanation is that the increased fall speed due to the increase
290 SRD cancels out with updrafts of the air parcels that cause the increased SRD in the first place.

291 Comparisons with LWC and the other previously discussed parameters (plots shown in the SI)
292 show no apparent correlation. Since the classification of SRD is only based on visual inspection,
293 no further numerical analysis was conducted and no fit parameters are presented.

298 4. Epitaxial Riming

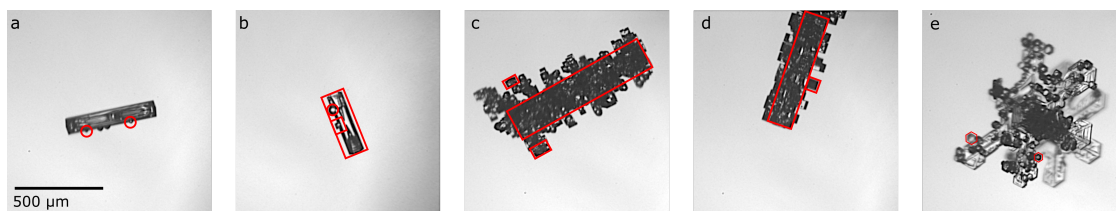
299 Rimed ice particles are usually understood as ice particles which have round accretion (rime).
300 However, during their ageing process, the form of accretion can change significantly. Fig. 7 shows
301 exemplary rimed ice particles with differently structured rime: round rime (Fig. 7a) and crystalline,
302 faceted rime (Fig. 7b-e). The latter can be explained by ageing (vapor deposition growth) of rimed
303 particles. In the following, round rime on ice particles will be referred to as "normal riming".



294 FIG. 6. The relative occurrence of particles of different riming degree as defined in Fig. 5: slight (purple),
295 moderate (yellow) and heavy riming (red) as well as graupel (blue) in correlation with ambient temperature (a),
296 ice particle size (b), and HCR Doppler velocity (c) similar to Fig. 2a-c. The values on the upper x-axis correspond
297 to the total number of particles per bin.

304 Particles with faceted rime have been reported in the past. Korolev et al. (2020) have reported a
305 case study with "a few ice particles with small faceted particles stuck to their surfaces" which they
306 refer to as "aged rimed ice particles" that had possibly originated from "vapor deposition regrowth
307 of rime into faceted particles". Libbrecht (2016) has reported "oriented freezing" of rimed droplets
308 that "freeze with their molecular lattices matching the pre-existing lattice underneath" which results
309 in "faceted rime particles". Since not all aged rimed particles show small faceted particles on the
310 surface and the attribute "faceted" is often used in other context for ice particles (pristine plates,
311 e.g. Libbrecht et al. (2015); Korolev et al. (2020)), we propose the term "*epitaxial riming*" to
312 avoid any confusion. In general, epitaxy refers to crystalline growth of a material on the surface of
313 another particle along the lattice structure of the underlying particle (Pashley 1956). The epitaxial
314 growth of ice on the surface of crystalline substrates, such as e.g. feldspar, has been the topic of
315 many previous works (e.g. Bryant et al. 1960; Kiselev et al. 2016). Here, we describe the growth
316 of small ice particles on the surface of larger ice particles along the same crystal axis. Thus, the
317 term "epitaxial riming" refers to faceted, rimed particles, underlining the important property that
318 the small "rimed" particles on the surface inherit the same lattice structure as the underlying host
319 particle and share the same c-axis as shown in Fig. 7.

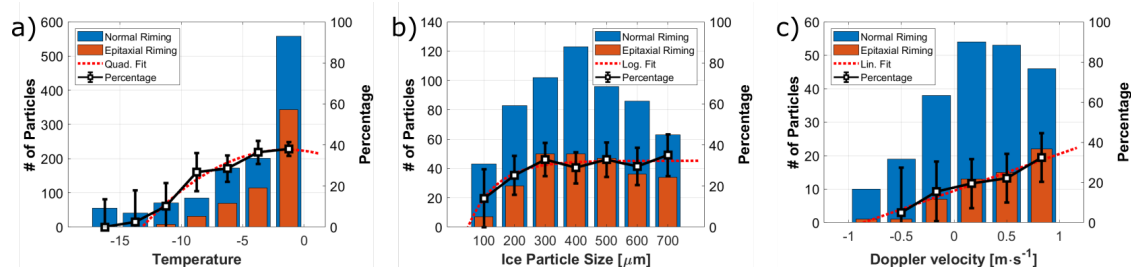
323 Multiple studies exist investigating the orientation of the freezing of rimed droplets, both in-vitro
324 (Magono and Aburakawa 1969; Takahashi 1979; Mizuno 1984; Mizuno and Wakahama 1983) and
325 in-situ (Uyeda and Kikuchi 1980). It has been shown that the crystal structure of rimed (still round)



320 FIG. 7. Exemplary rimed ice particles sampled during the IMPACTS campaign: "normally rimed" column
321 (a), column with both normal and epitaxial riming (b), heavily epitaxially rimed columns (c,d) and a epitaxially
322 rimed plate (e).

326 droplets matches the underlying lattice structure. At warm temperatures $-10 \leq T \leq 0^\circ\text{C}$, most small
327 droplets ($D \lesssim 40 \mu\text{m}$) freeze as single crystals whereas at colder temperatures ($T \leq -15^\circ\text{C}$), rimed
328 droplets tend to freeze as polycrystals. However, to our knowledge, so far no studies exist that
329 analyze the properties and formation conditions of the aforementioned epitaxially rimed particles.
330 In the following, we present detailed observations of such ice particles and propose that they are
331 the result of vapor deposition on rimed particles.

332 In Fig. 8, we show the relative occurrence of normally and epitaxially rimed particles during the
333 ACLOUD and SOCRATES campaign in correlation with ambient meteorological parameters. The
334 corresponding fit parameters for all histograms are shown in Tab. 2. Again, only particles sampled
335 at a temperature $T \geq -17^\circ\text{C}$ with diameter $D \geq 100 \mu\text{m}$ that were distinctively classified according
336 to the aforementioned manual classification are included.



337 FIG. 8. Absolute number of analyzed particles for normal (blue) and epitaxial (red) riming and fraction of
338 epitaxially rimed particles as a function of ambient temperature (a), ice particle size (b) and HCR Doppler
339 velocity (c).



340 Fig. 8a shows that there is a tendency to find more epitaxial riming at warmer temperatures near
341 $T = 0^{\circ}\text{C}$, where up to almost 40% of all rimed particles show epitaxial riming. Between -5 and
342 -10°C , the fraction of epitaxial riming slightly decreases from 40% to 30%. Below $T < -10^{\circ}\text{C}$, the
343 percentage of epitaxial riming decreases below 20%, although it should be noted that the statistics
344 for this temperature region are weak. This temperature dependency is in accordance with the
345 aforementioned studies showing that the rimed droplets tend to freeze as single crystals along the
346 c-axis of the underlying particle.

347 Fig. 8b shows a slight correlation of the occurrence of epitaxial particles with the size of the
348 underlying particle. For small particles below $D \leq 150 \mu\text{m}$, the fraction of epitaxially rimed
349 particles is 20%. This increases to up to 40% for ice particles larger than $D \geq 300 \mu\text{m}$. Above that,
350 the fraction of epitaxially rimed crystals is only weakly dependent of particle size. The correlation
351 of particle size with the presence of epitaxial riming can be explained by the fact that epitaxial
352 riming is caused by vapor deposition during the ageing process of rimed particles which naturally
353 also causes the particle to grow on their main surfaces.

354 Fig. 8c shows a trend towards higher upward vertical velocity, indicating a correlation with
355 updrafts. Again, comparisons with LWC and the other previously discussed parameters show no
356 significant correlation (plots shown in the SI).

357 Next, we will present a case study of a MPC sampled during the IMPACTS campaign. We
358 investigate the assumption that the ice particles with epitaxial riming are the result of ageing of
359 rimed particles and discuss its formation process.

TABLE 2. Fit parameters to the riming percentage histograms shown in Fig. 8.

	Fit function	R^2
Temperature	$y = -0.312 x^2 + -1.37 x + 36.6$	0.93
Ice particle diameter (PHIPS)	$y = 32.3 - \exp[-109 (x-367)]$	0.898
Vertical Doppler velocity (HCR)	$y = 15.5 x + 18$	0.856

360 *Case Study Feb01st - Epitaxial Riming on Columns*

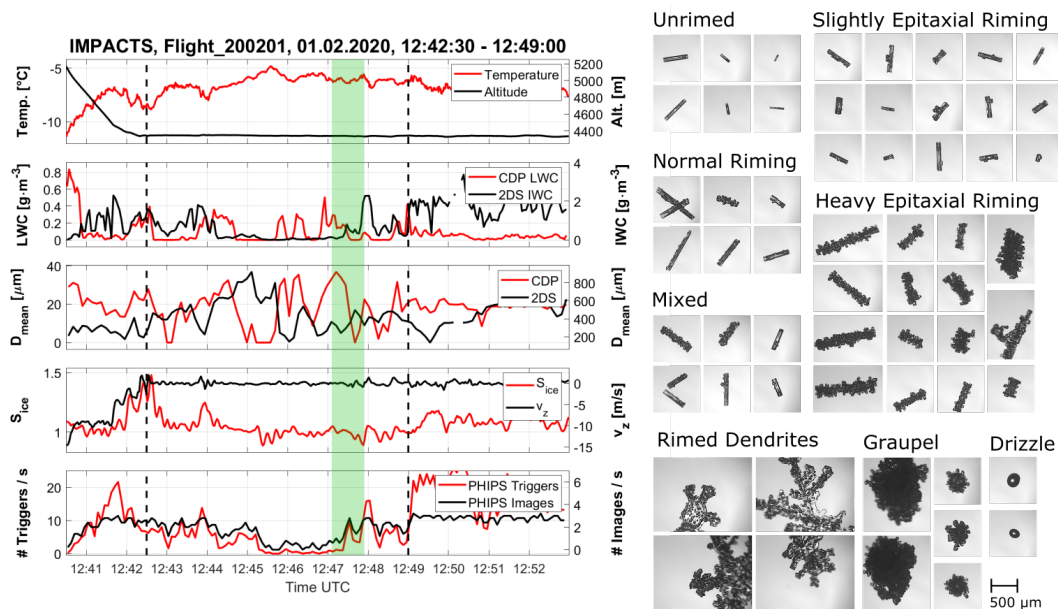
361 Fig. 9a shows meteorological and microphysical data collected on February 1st during the 2020
362 IMPACTS campaign. The MPC segment discussed in this case study was probed from 12:42:30 -
363 12:49:00 UTC ($\Delta t = 06:30$ min, which corresponds to $\Delta s = 58.5$ km) in an altitude of approximately
364 4,300 m at a temperature of about -12°C around $36^{\circ}\text{N}/73^{\circ}\text{W}$, roughly 300 km near the US east



365 coast. The vertical wind velocity was at a constant value around $\pm 0 \text{ m s}^{-1}$. The relative humidity
366 with respect to ice averaged about 100%. The liquid water content (LWC) measured with the
367 CDP averaged around 0.1 g m^{-3} and the total water content (TWC) measured with the 2DS was
368 around 0.5 g m^{-3} . The number-weighted mean particle diameter was around $20 \mu\text{m}$ for droplets and
369 between 200 to $800 \mu\text{m}$ for ice particles based on the measurements of CDP and 2D-S, respectively.

370 The trigger threshold of PHIPS was set in a way that the instrument started to trigger on droplets
371 with diameters larger than $D > 100 \mu\text{m}$. In this segment, in total, 1,589 particles were triggered
372 and 575 stereo images were acquired. Examples of stereo micrographs of particles from this flight
373 segment are shown in Fig. 9b. Of the 575 stereo images, 259 (45%) were not classified since they
374 were identified as potential shattering fragments smaller than $D = 100 \mu\text{m}$. Of the remaining ice
375 particles (320) most are classified as columnar particles (173) and 33 as needles. These particles
376 show a wide spectrum of riming degree, ranging from unrimed (43) to slightly (44), moderately
377 (42) and heavily rimed particles (124). We see different "types" of riming, most are epitaxially
378 rimed (87), 56 show normal riming. Furthermore, we see numerous particles with evidence of both
379 normal and epitaxial riming on the same particle (20), which we refer to as *mixed riming* in the
380 following. Apart from that, we see presence of 3 large drizzle droplets with diameters $200\text{--}300 \mu\text{m}$
381 as well as rimed dendrites (30) and graupel (48) particles. 35 particles were classified as irregulars.
382 Similar particle shapes are observed on the CPI imagery (not shown here).

389 The lower panel of Fig. 10 shows four exemplary ice particles that were sampled within a 45 s
390 window (12:47:07 - 12:47:52 UTC, corresponding to a distance of 6.7 km) that is indicated by the
391 shaded green area in Fig. 9. The particles that were sampled within this period show columnar
392 particles during different stages of the riming process: an unrimed (a), a normally rimed (b), a
393 mixed rimed (c) and epitaxially rimed column (d). Since we observe normal and epitaxial riming
394 not only within the same segment in near spatial vicinity, but also on the same singular particles,
395 we argue that normal and epitaxial riming are, as hypothesized, interlinked. As proposed by
396 Korolev et al. (2020), we argue that epitaxial riming is the result of the ageing (deposition growth)
397 of normally rimed particles as sketched in the upper panel of Fig. 10: An unrimed ice particle
398 (a) accretes a supercooled droplet and forms the initial primary "normal" riming (b). Ambient
399 water vapour deposits on the rime matching the lattice structure of the underlying particle and thus
400 forming the faceted surface. It is further possible that older rime grows on the expense of recently

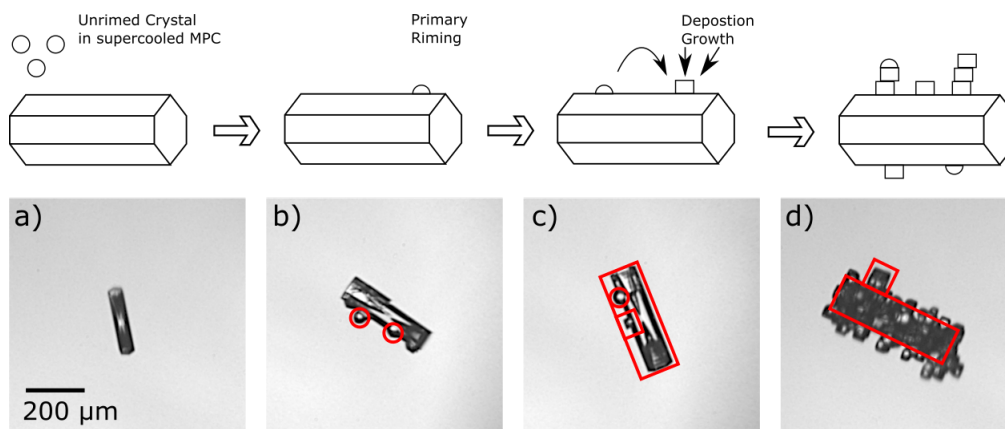


383 FIG. 9. Example of PHIPS data acquired in a mixed-phase cloud near the US east coast sampled during the
 384 IMPACTS campaign on February 1st, 2020. Left: overview of meteorological parameters, CDP liquid water
 385 content, 2D-S total water content, CDP and 2D-S number-weighted mean particle diameter and number of PHIPS
 386 images and total triggers. Right: representative PHIPS images of particles during the segment marked by the
 387 dashed black lines. The green shaded area marks a 45 s segment during which the four particles shown in Fig. 10
 388 were acquired.

401 accreted droplets that partly evaporate due to latent heat during the freezing process. More droplets
 402 are accreted such that normal and epitaxial riming can be observed on the same particle (c). The
 403 process repeats and the particle grows further until, eventually, the whole surface is covered by
 404 epitaxial rime (d).

409 5. Summary and Conclusion

410 In this work, we have presented in-situ observations using the PHIPS probe during three aircraft
 411 campaigns targeting MPCs in the Arctic, the Southern Ocean and US east coast. We have shown
 412 that riming is prevalent in the sampled clouds. We have manually classified ice particles in a
 413 size range from $100 \leq D \leq 700 \mu\text{m}$ and in the temperature range between $-17^\circ\text{C} \leq T \leq 0^\circ\text{C}$ regarding
 414 their riming status (rimed or unrimed) and surface riming degree (SRD). We show that riming is



405 FIG. 10. Schematic sketch of an epitaxially rimed column during different stages of the ageing process: unrimed
406 (a), normally rimed (b), mixed (c), and epitaxially rimed column (d). The lower panel shows corresponding
407 exemplary PHIPS images (#1309, #1325, #1320, and #1368) acquired within a 45 s segment in the presented
408 case-study (shaded green area in Fig. 9).

415 most prevalent at temperatures around -7°C , where, on average, 43% of the investigated particles
416 showed evidence of riming. We show that riming fraction increases with ice particle size (<20%
417 for $D \leq 200 \mu\text{m}$, 35-40% for $D \leq 400 \mu\text{m}$) and liquid water content (25% for $\text{LWC} \leq 0.05 \text{ g m}^{-3}$, up
418 to 60% for $\text{LWC} = 0.5 \text{ g m}^{-3}$).

419 We investigated riming features such as surface riming degree, size of rimed droplets and one-
420 sided riming based on visual inspection of individual stereo-images of ice particles imaged by
421 PHIPS during these campaigns. We show that the surface riming degree increases with decreasing
422 temperature and increasing ice particle size.

423 Furthermore, we have described ice particles with faceted, crystalline build-up which is aligned
424 to the lattice structure of the underlying particle. We call this "epitaxial riming" that we differentiate
425 from the round "normal riming". Epitaxial riming is most notable in the temperature range from
426 $-10^{\circ}\text{C} \leq T \leq 0^{\circ}\text{C}$ where epitaxial riming is visible on 32-37% of all rimed particles. We have
427 presented a case study that demonstrates that normal and epitaxial riming can be observed in
428 the same cloud segments and even simultaneously on the same single ice particles. We argue
429 that epitaxially rimed particles are the result of deposition growth of water vapor on primarily
430 rimed particles during their ageing process. However, further studies are needed to investigate
431 the exact growth mechanisms of epitaxial riming, for example in laboratory studies. Furthermore,



432 implications of epitaxial riming are still unclear. For example, it is unclear if epitaxial riming
433 affects rime splintering process and the splinter production rate.

434 Currently, the implications of riming towards the climate are not yet well understood as most
435 present day climate prediction models lack a parameterization of riming and consider riming only
436 for large particles ($D \geq 1$ mm) in the sense of graupel and snow. Riming on smaller particles is
437 usually not considered. The presented correlation between riming fraction and ambient meteorological
438 parameters can be used as a basis for first steps towards such a riming parameterization for
439 small or large scale models.

440 *Acknowledgments.* We express our gratitude all participants of the field studies for their efforts,
441 in particular the technical crew of the AWI Polar 6, NSF G-V and NASA P3. We would like to
442 acknowledge operational, technical and scientific support provided by NCAR's Earth Observing
443 Laboratory, sponsored by the National Science Foundation. We would also like to thank the
444 technical and scientific staff of IMK-AAF for their continuous support. This work has received
445 funding from the Helmholtz Research Program Atmosphere and Climate, by the German Research
446 Foundation (DFG grant JA 2818/1-1) and the Helmholtz Association's Initiative and Networking
447 Fund (grant agreement no. VH-NG-1531).

448 *Data availability statement.* The PHIPS single particle scattering data can be found online in
449 the PANGAEA database (<https://doi.org/10.1594/PANGAEA.902611>) for ACLOUD and the
450 EOL database (<https://doi.org/10.5065/D6639NKQ>) for SOCRATES. The single particle
451 microscopic stereo images from those two campaigns are available upon request from the authors.
452 The single particle microscopic stereo images from the IMPACTS campaign can be found in the
453 GHVR DAAC database (<http://dx.doi.org/10.5067/IMPACTS/PHIPS/DATA101>)

454 **References**

- 455 Abdelmonem, A., E. Järvinen, D. Duft, E. Hirst, S. Vogt, T. Leisner, and M. Schnaiter, 2016:
456 Phips–halo: the airborne particle habit imaging and polar scattering probe – part 1: Design and
457 operation. *Atmospheric Measurement Techniques*, **9** (7), 3131–3144, [https://doi.org/10.5194/](https://doi.org/10.5194/amt-9-3131-2016)
458 [amt-9-3131-2016](https://doi.org/10.5194/amt-9-3131-2016), URL <https://www.atmos-meas-tech.net/9/3131/2016/>.
- 459 Baltensperger, U., M. Schwikowski, D. Jost, S. Nyeki, H. Gäggeler, and O. Poulida, 1998: Scav-
460 ening of atmospheric constituents in mixed phase clouds at the high-alpine site jungfrau-



- 461 joch part i: Basic concept and aerosol scavenging by clouds. *Atmospheric Environment*,
462 **32 (23)**, 3975–3983, [https://doi.org/https://doi.org/10.1016/S1352-2310\(98\)00051-X](https://doi.org/https://doi.org/10.1016/S1352-2310(98)00051-X), URL
463 <https://www.sciencedirect.com/science/article/pii/S135223109800051X>.
- 464 Blahak, U., and A. Seifert, 2015: Cosmo / clm / art training course, langen, march 2015. URL
465 https://www.hzg.de/imperia/md/assets/clm/neu5_tl3.pdf.
- 466 Brientjes, R. T., A. J. Heymsfield, and T. W. Krauss, 1987: An examination of double-plate ice crys-
467 tals and the initiation of precipitation in continental cumulus clouds. *Journal of Atmospheric Sci-*
468 *ences*, **44 (9)**, 1331 – 1350, [https://doi.org/10.1175/1520-0469\(1987\)044<1331:AEODPI>2.0.](https://doi.org/10.1175/1520-0469(1987)044<1331:AEODPI>2.0.CO;2)
469 [CO;2](https://doi.org/10.1175/1520-0469(1987)044<1331:AEODPI>2.0.CO;2), URL [https://journals.ametsoc.org/view/journals/atsc/44/9/1520-0469_1987_044_1331_](https://journals.ametsoc.org/view/journals/atsc/44/9/1520-0469_1987_044_1331_aeodpi_2_0_co_2.xml)
470 [aeodpi_2_0_co_2.xml](https://journals.ametsoc.org/view/journals/atsc/44/9/1520-0469_1987_044_1331_aeodpi_2_0_co_2.xml).
- 471 Bryant, G., J. Hallett, and B. Mason, 1960: The epitaxial growth of ice on single-crystalline
472 substrates. *Journal of Physics and Chemistry of Solids*, **12 (2)**, 189–IN18, [https://doi.org/https://doi.org/10.1016/0022-3697\(60\)90036-6](https://doi.org/https://doi.org/10.1016/0022-3697(60)90036-6), URL [https://www.sciencedirect.com/science/article/](https://www.sciencedirect.com/science/article/pii/0022369760900366)
473 [pii/0022369760900366](https://www.sciencedirect.com/science/article/pii/0022369760900366), URL [https://www.sciencedirect.com/science/article/](https://www.sciencedirect.com/science/article/pii/0022369760900366)
474 [pii/0022369760900366](https://www.sciencedirect.com/science/article/pii/0022369760900366).
- 475 Ehrlich, A., and Coauthors, 2019: Collection of data sources for the Arctic CLOUD Observations
476 Using airborne measurements during polar Day (ACLOUD) campaign, North-West of Svalbard
477 between 23 May - 26 June 2017. PANGAEA, URL <https://doi.org/10.1594/PANGAEA.902603>,
478 <https://doi.org/10.1594/PANGAEA.902603>.
- 479 EOL, 2018: Socrates: Southern ocean clouds radiation aerosol transport experimental
480 study. UCAR/NCAR - Earth Observing Laboratory, URL [https://data.eol.ucar.edu/project/](https://data.eol.ucar.edu/project/SOCRATES)
481 [SOCRATES](https://data.eol.ucar.edu/project/SOCRATES).
- 482 Fan, J., S. Ghan, M. Ovchinnikov, X. Liu, P. J. Rasch, and A. Korolev, 2011: Rep-
483 resentation of arctic mixed-phase clouds and the wegener-bergeron-findeisen process in
484 climate models: Perspectives from a cloud-resolving study. *Journal of Geophysical*
485 *Research: Atmospheres*, **116 (D1)**, <https://doi.org/https://doi.org/10.1029/2010JD015375>,
486 URL <https://agupubs.onlinelibrary.wiley.com/doi/abs/10.1029/2010JD015375>, [https://agupubs.](https://agupubs.onlinelibrary.wiley.com/doi/pdf/10.1029/2010JD015375)
487 [onlinelibrary.wiley.com/doi/pdf/10.1029/2010JD015375](https://agupubs.onlinelibrary.wiley.com/doi/pdf/10.1029/2010JD015375).



- 488 Field, P. R., and Coauthors, 2017: *Secondary Ice Production - current state of the science and rec-*
489 *ommendations for the future*, Meteorological Monographs, Vol. 58, 7.1–7.20. American Mete-
490 rological Society, Boston (MA), <https://doi.org/10.1175/AMSMONOGRAPHS-D-16-0014.1>,
491 12.01.01; LK 01.
- 492 Garrett, T. J., and S. E. Yuter, 2014: Observed influence of riming, temperature, and tur-
493 bulence on the fallspeed of solid precipitation. *Geophysical Research Letters*, **41** (18),
494 6515–6522, <https://doi.org/https://doi.org/10.1002/2014GL061016>, URL <https://agupubs.onlinelibrary.wiley.com/doi/abs/10.1002/2014GL061016>, <https://agupubs.onlinelibrary.wiley.com/doi/pdf/10.1002/2014GL061016>.
- 497 Hallett, J., and S. C. Mossop, 1974: Production of secondary ice particles during
498 the riming process. *Nature*, **249** (5452), 26–28, [https://doi.org/https://doi.org/10.1038/](https://doi.org/https://doi.org/10.1038/249026a0)
499 [249026a0](https://doi.org/https://doi.org/10.1038/249026a0), URL <https://rmets.onlinelibrary.wiley.com/doi/abs/10.1002/qj.49710042514>, <https://rmets.onlinelibrary.wiley.com/doi/pdf/10.1002/qj.49710042514>.
- 501 Harimaya, T., 1975: The riming properties of snow crystals. *Journal of the Meteorological Society*
502 *of Japan. Ser. II*, **53** (6), 384–392, https://doi.org/10.2151/jmsj1965.53.6_384.
- 503 Hegg, D. A., A. D. Clarke, S. J. Doherty, and J. Ström, 2011: Measurements of black carbon aerosol
504 washout ratio on svalbard. *Tellus B*, **63** (5), 891–900, [https://doi.org/https://doi.org/10.1111/](https://doi.org/https://doi.org/10.1111/j.1600-0889.2011.00577.x)
505 [j.1600-0889.2011.00577.x](https://doi.org/https://doi.org/10.1111/j.1600-0889.2011.00577.x), URL [https://onlinelibrary.wiley.com/doi/abs/10.1111/j.1600-0889.](https://onlinelibrary.wiley.com/doi/abs/10.1111/j.1600-0889.2011.00577.x)
506 [2011.00577.x](https://onlinelibrary.wiley.com/doi/pdf/10.1111/j.1600-0889.2011.00577.x), <https://onlinelibrary.wiley.com/doi/pdf/10.1111/j.1600-0889.2011.00577.x>.
- 507 Herzegh, P. H., and P. V. Hobbs, 1980: The mesoscale and microscale structure and organization
508 of clouds and precipitation in midlatitude cyclones. ii: Warm-frontal clouds. *Journal of At-*
509 *mospheric Sciences*, **37** (3), 597 – 611, [https://doi.org/10.1175/1520-0469\(1980\)037<0597:](https://doi.org/10.1175/1520-0469(1980)037<0597:TMAMSA>2.0.CO;2)
510 [TMAMSA>2.0.CO;2](https://doi.org/10.1175/1520-0469(1980)037<0597:TMAMSA>2.0.CO;2), URL [https://journals.ametsoc.org/view/journals/atsc/37/3/1520-0469_](https://journals.ametsoc.org/view/journals/atsc/37/3/1520-0469_1980_037_0597_tmamsa_2_0_co_2.xml)
511 [1980_037_0597_tmamsa_2_0_co_2.xml](https://journals.ametsoc.org/view/journals/atsc/37/3/1520-0469_1980_037_0597_tmamsa_2_0_co_2.xml).
- 512 Järvinen, E., and Coauthors, 2018: Additional global climate cooling by clouds due to ice crystal
513 complexity. *Atmospheric Chemistry and Physics*, **18** (21), 15 767–15 781, [https://doi.org/10.](https://doi.org/10.5194/acp-18-15767-2018)
514 [5194/acp-18-15767-2018](https://doi.org/10.5194/acp-18-15767-2018), URL <https://www.atmos-chem-phys.net/18/15767/2018/>.



- 515 Järvinen, E., and Coauthors, 2021: Ice crystal complexity and link to cirrus cloud radiative effect.
516 *Journal of Geophysical Research: Atmospheres*, **2021**, in review.
- 517 Keppas, S. C., J. Crosier, T. W. Choulaton, and K. N. Bower, 2017: Ice lollies: An ice
518 particle generated in supercooled conveyor belts. *Geophysical Research Letters*, **44** (10),
519 5222–5230, <https://doi.org/https://doi.org/10.1002/2017GL073441>, URL <https://agupubs.onlinelibrary.wiley.com/doi/abs/10.1002/2017GL073441>, <https://agupubs.onlinelibrary.wiley.com/doi/pdf/10.1002/2017GL073441>.
- 522 Kikuchi, K., and H. Uyeda, 1979: Cloud droplets and rain drops collected and frozen on nat-
523 ural snow crystals. *Journal of the Meteorological Society of Japan. Ser. II*, **57** (3), 273–281,
524 https://doi.org/10.2151/jmsj1965.57.3_273.
- 525 Kiselev, A., F. Bachmann, P. Pedevilla, S. J. Cox, A. Michaelides, D. Gerthsen, and T. Leisner,
526 2016: Active sites in heterogeneous ice nucleation—the example of k-rich feldspars. *Science*,
527 <https://doi.org/10.1126/science.aai8034>, URL <https://science.sciencemag.org/content/early/2016/12/07/science.aai8034>, <https://science.sciencemag.org/content/early/2016/12/07/science.aai8034.full.pdf>.
- 530 Kneifel, S., and D. Moisseev, 2020: Long-term statistics of riming in nonconvective clouds derived
531 from ground-based doppler cloud radar observations. *Journal of the Atmospheric Sciences*,
532 **77** (10), 3495 – 3508, <https://doi.org/10.1175/JAS-D-20-0007.1>, URL <https://journals.ametsoc.org/view/journals/atsc/77/10/jasD200007.xml>.
- 534 Knudsen, E. M., and Coauthors, 2018: Meteorological conditions during the acloud/pascal
535 field campaign near svalbard in early summer 2017. *Atmospheric Chemistry and Physics*,
536 **18** (24), 17 995–18 022, <https://doi.org/10.5194/acp-18-17995-2018>, URL <https://www.atmos-chem-phys.net/18/17995/2018/>.
- 538 Korolev, A., and Coauthors, 2017: Mixed-phase clouds: Progress and challenges. *Meteoro-*
539 *logical Monographs*, **58**, 5.1–5.50, <https://doi.org/10.1175/AMSMONOGRAPHS-D-17-0001.1>, URL <https://doi.org/10.1175/AMSMONOGRAPHS-D-17-0001.1>, <https://doi.org/10.1175/AMSMONOGRAPHS-D-17-0001.1>.



- 542 Korolev, A., and Coauthors, 2020: A new look at the environmental conditions favorable to sec-
543 ondary ice production. *Atmospheric Chemistry and Physics*, **20** (3), 1391–1429, [https://doi.org/](https://doi.org/10.5194/acp-20-1391-2020)
544 10.5194/acp-20-1391-2020, URL <https://acp.copernicus.org/articles/20/1391/2020/>.
- 545 Leinonen, J., and W. Szyrmer, 2015: Radar signatures of snowflake riming: A
546 modeling study. *Earth and Space Science*, **2** (8), 346–358, [https://doi.org/https://doi.](https://doi.org/https://doi.org/10.1002/2015EA000102)
547 [org/10.1002/2015EA000102](https://doi.org/10.1002/2015EA000102), URL [https://agupubs.onlinelibrary.wiley.com/doi/abs/10.1002/](https://agupubs.onlinelibrary.wiley.com/doi/abs/10.1002/2015EA000102)
548 [2015EA000102](https://agupubs.onlinelibrary.wiley.com/doi/pdf/10.1002/2015EA000102), <https://agupubs.onlinelibrary.wiley.com/doi/pdf/10.1002/2015EA000102>.
- 549 Leinonen, J., and Coauthors, 2018: Retrieval of snowflake microphysical properties from mul-
550 tiframe radar observations. *Atmospheric Measurement Techniques*, **11** (10), 5471–5488,
551 <https://doi.org/10.5194/amt-11-5471-2018>, URL [https://amt.copernicus.org/articles/11/5471/](https://amt.copernicus.org/articles/11/5471/2018/)
552 2018/.
- 553 Libbrecht, K., 2016: *Ken Libbrecht's Field Guide to Snowflakes*. Voyageur Press, URL [https://](https://books.google.de/books?id=eOv83aUgOvwC)
554 books.google.de/books?id=eOv83aUgOvwC.
- 555 Libbrecht, K., C. Miller, R. Potter, N. Budaeva, C. Lemon, and S. Thomas, 2015: Toward a
556 comprehensive model of snow crystal growth: 4. measurements of diffusion-limited growth at
557 -15 c.
- 558 Lin, Y., L. Donner, and B. Colle, 2011: Parameterization of riming intensity and its impact on ice
559 fall speed using arm data. *Monthly Weather Review - MON WEATHER REV*, **139**, 1036–1047,
560 <https://doi.org/10.1175/2010MWR3299.1>.
- 561 Locatelli, J. D., and P. V. Hobbs, 1974: Fall speeds and masses of solid precipitation
562 particles. *Journal of Geophysical Research (1896-1977)*, **79** (15), 2185–2197, [https://doi.org/](https://doi.org/https://doi.org/10.1029/JC079i015p02185)
563 <https://doi.org/10.1029/JC079i015p02185>, URL [https://agupubs.onlinelibrary.wiley.com/doi/](https://agupubs.onlinelibrary.wiley.com/doi/abs/10.1029/JC079i015p02185)
564 [abs/10.1029/JC079i015p02185](https://agupubs.onlinelibrary.wiley.com/doi/pdf/10.1029/JC079i015p02185), [https://agupubs.onlinelibrary.wiley.com/doi/pdf/10.1029/](https://agupubs.onlinelibrary.wiley.com/doi/pdf/10.1029/JC079i015p02185)
565 [JC079i015p02185](https://agupubs.onlinelibrary.wiley.com/doi/pdf/10.1029/JC079i015p02185).
- 566 Magono, C., and H. Aburakawa, 1969: Experimental studies on snow crystals of plane type with
567 spatial branches. *Journal of the Faculty of Science, Hokkaido University. Series 7, Geophysics*,
568 **3** (2), 85–97, URL <http://hdl.handle.net/2115/8680>.



- 569 Magono, C., and C. W. Lee, 1966: Meteorological classification of natural snow crystals. *Journal*
570 *of the Faculty of Science, Hokkaido University. Series 7, Geophysics*, **2** (4), 321–335, URL
571 <http://hdl.handle.net/2115/8672>.
- 572 Mason, S. L., C. J. Chiu, R. J. Hogan, D. Moisseev, and S. Kneifel, 2018: Retrievals of riming
573 and snow density from vertically pointing doppler radars. *Journal of Geophysical Research:*
574 *Atmospheres*, **123** (24), 13,807–13,834, <https://doi.org/https://doi.org/10.1029/2018JD028603>,
575 URL <https://agupubs.onlinelibrary.wiley.com/doi/abs/10.1029/2018JD028603>, <https://agupubs.onlinelibrary.wiley.com/doi/pdf/10.1029/2018JD028603>.
- 577 McCoy, D. T., I. Tan, D. L. Hartmann, M. D. Zelinka, and T. Storelvmo,
578 2016: On the relationships among cloud cover, mixed-phase partitioning, and
579 planetary albedo in gcms. *Journal of Advances in Modeling Earth Systems*,
580 **8** (2), 650–668, <https://doi.org/10.1002/2015MS000589>, URL <https://agupubs.onlinelibrary.wiley.com/doi/abs/10.1002/2015MS000589>, <https://agupubs.onlinelibrary.wiley.com/doi/pdf/10.1002/2015MS000589>.
- 583 McFarquhar, G. M., and Coauthors, 2019: Airborne, ship-, and ground-based observations of
584 clouds, aerosols, and precipitation from recent field projects over the southern ocean. *99th annual meeting, American Meteorological Society*, URL <https://ams.confex.com/ams/2019Annual/meetingapp.cgi/Paper/350863>.
- 587 McMurdie, L., G. Heymsfield, J. Yorks, and S. Braun, 2019: Investigation of microphysics and
588 precipitation for atlantic coast-threatening snowstorms (impacts) collection. NASA EOSDIS
589 Global Hydrology Resource Center Distributed, Active Archive Center, Huntsville, Alabama,
590 U.S.A., URL <http://dx.doi.org/10.5067/IMPACTS/DATA101>.
- 591 Mizuno, Y., 1984: Epitaxial freezing of supercooled droplets on ice surfaces. *Contributions from*
592 *the Institute of Low Temperature Science*, **A33**, 1–27, URL <http://hdl.handle.net/2115/20248>.
- 593 Mizuno, Y., and G. Wakahama, 1983: Structure and orientation of frozen droplets on ice surfaces.
594 *The Journal of Physical Chemistry*, **87** (21), 4161–4167, <https://doi.org/10.1021/j100244a037>,
595 URL <https://doi.org/10.1021/j100244a037>, <https://doi.org/10.1021/j100244a037>.



- 596 Mosimann, L., 1995: An improved method for determining the degree of snow crystal
597 riming by vertical doppler radar. *Atmospheric Research*, **37** (4), 305–323, [https://doi.org/](https://doi.org/https://doi.org/10.1016/0169-8095(94)00050-N)
598 [https://doi.org/10.1016/0169-8095\(94\)00050-N](https://doi.org/10.1016/0169-8095(94)00050-N), URL [https://www.sciencedirect.com/science/](https://www.sciencedirect.com/science/article/pii/016980959400050N)
599 [article/pii/016980959400050N](https://www.sciencedirect.com/science/article/pii/016980959400050N).
- 600 Mosimann, L., M. Steiner, J. Collett, and et al., 1993: Ice crystal observations and the degree
601 of riming in winter precipitation. *Water Air Soil Pollution*, **68**, 29–42, <https://doi.org/https://doi.org/10.1007/BF00479391>.
602
- 603 Mosimann, L., E. Weingartner, and A. Waldvogel, 1994: An analysis of accreted
604 drop sizes and mass on rimed snow crystals. *Journal of Atmospheric Sciences*,
605 **51** (11), 1548 – 1558, [https://doi.org/10.1175/1520-0469\(1994\)051<1548:AAOADS>2.0.CO;](https://doi.org/10.1175/1520-0469(1994)051<1548:AAOADS>2.0.CO;2)
606 [2](https://doi.org/10.1175/1520-0469(1994)051<1548:AAOADS>2.0.CO;2), URL [https://journals.ametsoc.org/view/journals/atsc/51/11/1520-0469_1994_051_1548_](https://journals.ametsoc.org/view/journals/atsc/51/11/1520-0469_1994_051_1548_aaoads_2_0_co_2.xml)
607 [aaoads_2_0_co_2.xml](https://journals.ametsoc.org/view/journals/atsc/51/11/1520-0469_1994_051_1548_aaoads_2_0_co_2.xml).
- 608 Ono, A., 1969: The shape and riming properties of ice crystals in natural clouds. *Journal of At-*
609 *mospheric Sciences*, **26** (1), 138 – 147, [https://doi.org/10.1175/1520-0469\(1969\)026<0138:](https://doi.org/10.1175/1520-0469(1969)026<0138:TSARPO>2.0.CO;2)
610 [TSARPO>2.0.CO;2](https://doi.org/10.1175/1520-0469(1969)026<0138:TSARPO>2.0.CO;2), URL [https://journals.ametsoc.org/view/journals/atsc/26/1/1520-0469_](https://journals.ametsoc.org/view/journals/atsc/26/1/1520-0469_1969_026_0138_tsarpo_2_0_co_2.xml)
611 [1969_026_0138_tsarpo_2_0_co_2.xml](https://journals.ametsoc.org/view/journals/atsc/26/1/1520-0469_1969_026_0138_tsarpo_2_0_co_2.xml).
- 612 Ovchinnikov, M., and Coauthors, 2014: Intercomparison of large-eddy simulations of
613 arctic mixed-phase clouds: Importance of ice size distribution assumptions. *Jour-*
614 *nal of Advances in Modeling Earth Systems*, **6** (1), 223–248, [https://doi.org/https://doi.](https://doi.org/https://doi.org/10.1002/2013MS000282)
615 [org/10.1002/2013MS000282](https://doi.org/10.1002/2013MS000282), URL [https://agupubs.onlinelibrary.wiley.com/doi/abs/10.1002/](https://agupubs.onlinelibrary.wiley.com/doi/abs/10.1002/2013MS000282)
616 [2013MS000282](https://agupubs.onlinelibrary.wiley.com/doi/abs/10.1002/2013MS000282), <https://agupubs.onlinelibrary.wiley.com/doi/pdf/10.1002/2013MS000282>.
- 617 Pashley, D., 1956: The study of epitaxy in thin surface films. *Advances in Physics*,
618 **5** (18), 173–240, <https://doi.org/10.1080/00018735600101175>, URL [https://doi.org/10.1080/](https://doi.org/10.1080/00018735600101175)
619 [00018735600101175](https://doi.org/10.1080/00018735600101175), <https://doi.org/10.1080/00018735600101175>.
- 620 Rango, A., J. Foster, E. G. Josberger, E. F. Erbe, W. P. Wergin, and C. Pooley, 2003:
621 Rime and graupel: Description and characterization as revealed by low-temperature scan-
622 ning electron microscopy. *Scanning*, **25** (3), 121–131, [https://doi.org/https://doi.org/10.1002/](https://doi.org/https://doi.org/10.1002/sca.4950250304)
623 [sca.4950250304](https://doi.org/10.1002/sca.4950250304), URL <https://onlinelibrary.wiley.com/doi/abs/10.1002/sca.4950250304>, <https://onlinelibrary.wiley.com/doi/pdf/10.1002/sca.4950250304>, <https://onlinelibrary.wiley.com/doi/pdf/10.1002/sca.4950250304>.



- 625 Saleeby, S. M., and W. R. Cotton, 2008: A binned approach to cloud-droplet riming imple-
626 mented in a bulk microphysics model. *Journal of Applied Meteorology and Climatology*, **47** (2),
627 694 – 703, <https://doi.org/10.1175/2007JAMC1664.1>, URL [https://journals.ametsoc.org/view/
628 journals/apme/47/2/2007jamc1664.1.xml](https://journals.ametsoc.org/view/journals/apme/47/2/2007jamc1664.1.xml).
- 629 Schnaiter, M., E. Järvinen, A. Abdelmonem, and T. Leisner, 2018: Phips-halo: the airborne parti-
630 cle habit imaging and polar scattering probe – part 2: Characterization and first results. *Atmo-
631 spheric Measurement Techniques*, **11** (1), 341–357, <https://doi.org/10.5194/amt-11-341-2018>,
632 URL <https://www.atmos-meas-tech.net/11/341/2018/>.
- 633 Schnaiter, M., and Coauthors, 2016: Cloud chamber experiments on the origin of ice crystal com-
634 plexity in cirrus clouds. *Atmospheric Chemistry and Physics*, **16** (8), 5091–5110, [https://doi.org/
635 10.5194/acp-16-5091-2016](https://doi.org/10.5194/acp-16-5091-2016), URL <https://acp.copernicus.org/articles/16/5091/2016/>.
- 636 Schön, R., and Coauthors, 2011: Particle habit imaging using incoherent light: A first step toward
637 a novel instrument for cloud microphysics. *Journal of Atmospheric and Oceanic Technology*,
638 **28** (4), 493–512, <https://doi.org/10.1175/2011JTECHA1445.1>, URL [https://doi.org/10.1175/
639 2011JTECHA1445.1](https://doi.org/10.1175/2011JTECHA1445.1), <https://doi.org/10.1175/2011JTECHA1445.1>.
- 640 Stevens, R. G., and Coauthors, 2018: A model intercomparison of ccn-limited tenuous clouds in
641 the high arctic. *Atmospheric Chemistry and Physics*, **18** (15), 11 041–11 071, [https://doi.org/
642 10.5194/acp-18-11041-2018](https://doi.org/10.5194/acp-18-11041-2018), URL <https://acp.copernicus.org/articles/18/11041/2018/>.
- 643 Takahashi, C., 1979: Formation of poly-crystalline snow crystals by riming process. *Journal of the
644 Meteorological Society of Japan. Ser. II*, **57** (5), 458–464, [https://doi.org/10.2151/jmsj1965.57.
645 5_458](https://doi.org/10.2151/jmsj1965.57.5_458).
- 646 UCAR/NCAR-EOL, 2018: Near her radar and hsrl lidar moments data. version 1.0. ucar/ncar -
647 earth observing laboratory. URL <https://doi.org/10.5065/D64J0CZS>.
- 648 Uyeda, H., and K. Kikuchi, 1978: Freezing experiment of supercooled water droplets frozen by
649 using single crystal ice. *Journal of the Meteorological Society of Japan. Ser. II*, **56** (1), 43–51,
650 https://doi.org/10.2151/jmsj1965.56.1_43.



- 651 Uyeda, H., and K. Kikuchi, 1980: Measurements of the principal axis of frozen hemispheric water
652 droplets. *Journal of the Meteorological Society of Japan. Ser. II*, **58 (1)**, 52–58, [https://doi.org/](https://doi.org/10.2151/jmsj1965.58.1_52)
653 10.2151/jmsj1965.58.1_52.
- 654 Waitz, F., M. Schnaiter, T. Leisner, and E. Järvinen, 2021: Phips-halo: the airborne particle habit
655 imaging and polar scattering probe – part 3: Single particle phase discrimination and particle
656 size distribution based on angular scattering function. *Atmospheric Measurement Techniques*
657 *Discussions*, **2021**, 1–28, <https://doi.org/10.5194/amt-2020-297>, URL [https://amt.copernicus.](https://amt.copernicus.org/preprints/amt-2020-297/)
658 [org/preprints/amt-2020-297/](https://amt.copernicus.org/preprints/amt-2020-297/).
- 659 Wang, P. K., and W. Ji, 2000: Collision efficiencies of ice crystals at low–intermediate reynolds
660 numbers colliding with supercooled cloud droplets: A numerical study. *Journal of the At-*
661 *mospheric Sciences*, **57 (8)**, 1001 – 1009, [https://doi.org/10.1175/1520-0469\(2000\)057<1001:](https://doi.org/10.1175/1520-0469(2000)057<1001:CEOICA>2.0.CO;2)
662 [CEOICA>2.0.CO;2](https://doi.org/10.1175/1520-0469(2000)057<1001:CEOICA>2.0.CO;2), URL [https://journals.ametsoc.org/view/journals/atmsc/57/8/1520-0469_](https://journals.ametsoc.org/view/journals/atmsc/57/8/1520-0469_2000_057_1001_ceoica_2.0.co_2.xml)
663 [2000_057_1001_ceoica_2.0.co_2.xml](https://journals.ametsoc.org/view/journals/atmsc/57/8/1520-0469_2000_057_1001_ceoica_2.0.co_2.xml).
- 664 Wendisch, M., A. Macke, A. Ehrlich, C. Lüpkes, and Coauthors, 2019: **100 (5)**, 841–871,
665 <https://doi.org/10.1175/BAMS-D-18-0072.1>, URL [https://doi.org/10.1175/BAMS-D-18-0072.](https://doi.org/10.1175/BAMS-D-18-0072.1)
666 [1](https://doi.org/10.1175/BAMS-D-18-0072.1), <https://doi.org/10.1175/BAMS-D-18-0072.1>.
- 667 Ávila, E. E., N. E. Castellano, C. P. R. Saunders, R. E. Bürgesser, and G. G. Aguirre Varela,
668 2009: Initial stages of the riming process on ice crystals. *Geophysical Research Let-*
669 *ters*, **36 (9)**, <https://doi.org/https://doi.org/10.1029/2009GL037723>, URL [https://agupubs.](https://agupubs.onlinelibrary.wiley.com/doi/abs/10.1029/2009GL037723)
670 [onlinelibrary.wiley.com/doi/abs/10.1029/2009GL037723](https://agupubs.onlinelibrary.wiley.com/doi/abs/10.1029/2009GL037723), [https://agupubs.onlinelibrary.wiley.](https://agupubs.onlinelibrary.wiley.com/doi/pdf/10.1029/2009GL037723)
671 [com/doi/pdf/10.1029/2009GL037723](https://agupubs.onlinelibrary.wiley.com/doi/pdf/10.1029/2009GL037723).